

Detection of Al II in the Ultraviolet Spectra of Metal-Poor Stars: An Empirical LTE Test of NLTE Aluminum Abundance Calculations*

IAN U. ROEDERER^{1,2} AND JAMES E. LAWLER³

¹*Department of Astronomy, University of Michigan, 1085 S. University Ave., Ann Arbor, MI 48109, USA*

²*Joint Institute for Nuclear Astrophysics – Center for the Evolution of the Elements (JINA-CEE), USA*

³*Department of Physics, University of Wisconsin – Madison, 1150 University Ave., Madison, WI 53706, USA*

ABSTRACT

We report the detection of an Al II line at 2669.155 Å in 11 metal-poor stars, using ultraviolet spectra obtained with the Space Telescope Imaging Spectrograph on board the Hubble Space Telescope. We derive Al abundances from this line using a standard abundance analysis, assuming local thermodynamic equilibrium (LTE). The mean [Al/Fe] ratio is -0.06 ± 0.04 ($\sigma = 0.22$) for these 11 stars spanning $-3.9 < [\text{Fe}/\text{H}] < -1.3$, or $[\text{Al}/\text{Fe}] = -0.10 \pm 0.04$ ($\sigma = 0.18$) for 9 stars spanning $-3.0 < [\text{Fe}/\text{H}] < -1.3$ if two carbon-enhanced stars are excluded. We use these abundances to perform an empirical test of non-LTE (NLTE) abundance corrections predicted for resonance lines of Al I, including the commonly-used optical Al I line at 3961 Å. The Al II line is formed in LTE, and the abundance derived from this line matches that derived from high-excitation Al I lines predicted to have minimal NLTE corrections. The differences between the abundance derived from the Al II line and the LTE abundance derived from Al I resonance lines are +0.4 to +0.9 dex, which match the predicted NLTE corrections for the Al I resonance lines. We conclude that the NLTE abundance calculations are approximately correct and should be applied to LTE abundances derived from Al I lines.

Keywords: Nucleosynthesis (1131); Stellar abundances (1577); Stellar atmospheres (1584); Ultraviolet astronomy (1736)

1. INTRODUCTION

The element aluminum (Al, $Z = 13$) is commonly found in stars. Al is produced mainly during hydrostatic carbon burning, with additional contributions from neon burning, in massive stars (e.g., Arnett & Thielemann 1985; Thielemann & Arnett 1985; Woosley & Weaver 1995). Al is produced during α -, n -, and p -capture reaction sequences starting from the neutron-rich seed nuclei ^{22}Ne and ^{23}Na . Theoretically Al has some characteristics of a “primary” element, in that the [Al/Fe] ratios are independent of the initial metallicities of the

stars where Al is produced, because its seed nuclei are themselves produced during the normal course of stellar burning in massive stars. Al also has a “secondary” metallicity dependence, because these seed nuclei may also be present initially, thus amplifying Al production. In Galactic chemical evolution models, the [Al/Fe] ratio is generally flat or shows a mild increase with increasing [Fe/H] (e.g., Timmes et al. 1995; Kobayashi et al. 2006, 2020; Romano et al. 2010).

Unfortunately, the method of analyzing Al lines in stellar spectra greatly influences the derived abundances and thus our understanding of Al nucleosynthesis. Al abundances in metal-poor stars were initially found to exhibit a strong secondary behavior, sub-solar at low metallicity and approaching or even exceeding the solar ratio at higher metallicity (e.g., Peterson 1978; Magain 1987; Gratton & Sneden 1988; McWilliam et al. 1995; Ryan et al. 1996; Chen et al. 2000). Those results were based on the assumption that the excitation and ionization could be adequately described by local thermodynamic equilibrium (LTE). Applying non-LTE (NLTE) calculations, in contrast, yields [Al/Fe] ratios much closer to the solar ratio across a wide range of metallicities ($-4 < [\text{Fe}/\text{H}] < 0$; e.g., Baumüller & Gehren 1997; Gehren et al. 2004; Andrievsky et al.

Email: iur@umich.edu

* Based on observations made with the NASA/ESA *Hubble Space Telescope*, obtained at the Space Telescope Science Institute, which is operated by the Association of Universities for Research in Astronomy, Inc. under NASA contract NAS 5-26555. The data presented in this paper were obtained from the Barbara A. Mikulski Archive for Space Telescopes. Other data have been obtained from the European Southern Observatory Science Archive Facility. This research has also made use of the Keck Observatory Archive, which is operated by the W.M. Keck Observatory and the NASA Exoplanet Science Institute, under contract with NASA. This paper includes data taken at The McDonald Observatory of The University of Texas at Austin, and the the 6.5 meter Magellan Telescopes located at Las Campanas Observatory, Chile.

2008). Consequently, the NLTE Al abundances better match the theoretically-predicted behavior.

The choice of which Al spectral lines to use also has an outsized influence on the derived Al abundances. It has long been discussed (e.g., [Francois 1986](#); [Gratton & Sneden 1988](#); [Ryan et al. 1996](#)) whether high-excitation Al I lines in the red (e.g., $\lambda 6696, 6698 \text{ \AA}$) yield abundances higher than the resonance Al I lines in the blue ($\lambda 3944, 3961 \text{ \AA}$). Observational errors were once large enough to sustain this debate. Modern analyses (e.g., [Mashonkina et al. 2016](#); [Zhao et al. 2016](#); [Nordlander & Lind 2017](#)) have shown conclusively that the high-excitation lines yield abundances higher by several tenths of a dex than the resonance lines. Several sets of high-excitation Al I lines yield reliable abundances in LTE, yet only the blue resonance lines are detected in warm or metal-poor stars. This situation presents a challenge for interpreting Al abundances in stars spanning a wide range of temperatures and metallicities.

We have identified an Al II absorption line at 2669.155 \AA in the ultraviolet (UV) spectra of several metal-poor stars. This line is relatively unblended, and to the best of our knowledge it has not been used previously to derive Al abundances. It arises from the $2p^6 3s$ ground state of Al^+ , and it is the only line connected to the Al^+ ground level that is detectable in near-UV, optical, or near-infrared spectra.

The first ionization potential of Al is low, 5.99 eV, and the second ionization potential is high, 18.83 eV, so Al^+ is the dominant ionization state of Al in the atmospheres of metal-poor stars. Abundances derived from the UV Al II line, which should be formed in LTE ([Mashonkina et al. 2016](#)), can be used to empirically assess the deviations from LTE of transitions in neutral Al. Similar tests have been performed previously for other elements. The most extensive studies have focused on iron-group elements (e.g., [Sneden et al. 2016](#); [Roederer & Barklem 2018](#); [Cowan et al. 2020](#)). Some have examined the α elements Mg ([Spite et al. 2017](#)) and Ca ([Den Hartog et al. 2021](#)), while others have examined neutron-capture elements (e.g., [Roederer & Lawler 2012](#); [Peterson et al. 2020](#); [Roederer et al. 2020](#)). UV spectra collected with the Hubble Space Telescope (HST) are crucial to this work because many of the lines arising in ionized atoms are found in the UV, below the atmospheric cutoff near 3000 \AA .

In this paper, we present an analysis of Al I and II lines in metal-poor stars. We compare Al abundances derived from UV and optical Al I and II lines as a test of the NLTE predictions, and we present $[\text{Al}/\text{Fe}]$ ratios for this sample of metal-poor stars. We define the Al abundance as $\log \varepsilon(\text{Al}) \equiv \log_{10}(N_{\text{Al}}/N_{\text{H}}) + 12.0$. We define the abundance ratio of Al and Fe relative to the Solar ratio as $[\text{Al}/\text{Fe}] \equiv \log_{10}(N_{\text{Al}}/N_{\text{Fe}}) - \log_{10}(N_{\text{Al}}/N_{\text{Fe}})_{\odot}$, where $\log \varepsilon(\text{Al})_{\odot} = 6.45$ and $\log \varepsilon(\text{Fe})_{\odot} = 7.50$ ([Asplund et al. 2009](#)). By convention, abundances or ratios denoted with the ionization state are understood to be the

total elemental abundance as derived from transitions of that particular ionization state after Saha ionization corrections have been applied.

2. ATOMIC DATA

The one stable isotope of Al, ^{27}Al , has non-zero nuclear spin, $I = 5/2$, which produces hyperfine structure (HFS) splitting in the electronic energy levels. We reconstruct the HFS splitting of the Al II line at 2669 \AA using the HFS magnetic dipole, A , and electric quadrupole, B , constants for the upper $3s3p \ ^3P_1^o$ level; these values are 0 for the lower $2p^6 3s^2 \ ^1S_0$ level. We calculate the HFS A and B values that reproduce the splittings measured by [Itano et al. \(2007\)](#), $A = 1339.311 \text{ MHz}$ and $B = -21.606 \text{ MHz}$. Two measured splittings and two adjustable constants yield a perfect fit. However, [Itano et al.](#) mention that the second-order magnetic dipole energy is comparable to the first-order electric quadrupole energy. Any comparison of these HFS constants to ab-initio theory requires some care, especially for the HFS B constant. The above A value agrees to better than 1% with the ab-initio theoretical result from [Zhang et al. \(2017\)](#), $A = 1327.3 \pm 10.2 \text{ MHz}$. The above B value does not agree as well with the result from [Zhang et al.](#), $B = -15.1 \pm 0.2 \text{ MHz}$, but B values are generally not important in astrophysical research. There is no doubt that the splitting measurements from [Itano et al.](#), made to kHz accuracy, are better than theoretical values for the HFS A and B . We normalize the HFS line component shifts to the center-of-gravity wavelength calculated from the National Institute of Standards and Technology (NIST) energy levels. The relative strengths of each component are calculated using the LS angular momentum coupling formulae presented in [Condon & Shortley \(1935\)](#). Table 1 presents the HFS line component pattern.

The NIST Atomic Spectra Database (ASD, version 5.8; [Kramida et al. 2020](#)) recommends a $\log(gf)$ value of -4.979 for the Al II line at 2669 \AA ([Träbert et al. 1999](#)), with a grade of “A+” (uncertainty $< 2\%$). We adopt this value.

We also examine 15 Al I lines. The UV Al I lines were selected for analysis based on their detectability and relative lack of blends in the spectra of HD 84937 and HD 222925 (see Section 3). For each line, Table 2 lists the wavelength, excitation potential (E.P.) of the lower level, $\log(gf)$ value, NIST ASD grade on the accuracy of the $\log(gf)$ value, and source of the HFS line component pattern. HFS patterns are available for nine of these lines in the Vienna Atomic Line Database (VALD3; [Piskunov et al. 1995](#); [Pakhomov et al. 2019](#)), which makes use of data presented in [Stück & Zimmermann \(1970\)](#), [Falkenberg & Zimmermann \(1979\)](#), [Zhan-Kui et al. \(1982\)](#), [Belfrage et al. \(1984\)](#), [Jönsson et al. \(1984\)](#), [Biemont & Brault \(1987\)](#), [Chang \(1990\)](#), and [Brown & Evenson \(1999\)](#). We adopt the NIST ASD recommended $\log(gf)$ values for the Al I lines, which

Table 1. Hyperfine Structure for the $^{27}\text{Al II}$ Line at 2669 Å

Wavenumber (cm^{-1})	λ_{air} (Å)	F_{upper}	F_{lower}	Component Position (cm^{-1})	Component Position (Å)	Strength
37453.91	2669.155	3.5	2.5	+0.1115	-0.00795	0.4444
37453.91	2669.155	2.5	2.5	-0.0441	+0.00314	0.3333
37453.91	2669.155	1.5	2.5	-0.1569	+0.01118	0.2222

NOTE—Energy levels from the NIST ASD and the index of air (Peck & Reeder 1972) are used to compute the center-of-gravity wavenumbers and air wavelengths, λ_{air} . Line component positions are given relative to those values.

are based on data presented in Davidson et al. (1990), Mendoza et al. (1995), and Hannaford (1999). We include damping constants for collisional broadening with neutral hydrogen from Barklem et al. (2000), when available, otherwise we adopt the broadening as described by the Unsöld (1955) recipe in our spectrum synthesis calculations.

3. ARCHIVAL OBSERVATIONS

We collect archival UV and optical spectra for 11 stars where the Al II line is detected and useful for analysis. Table 3 lists the basic characteristics of these spectra, including the instrument used, program identification (ID) number, datasets, original principle investigator (PI) of the observations, wavelength (λ) coverage, and spectral resolving power ($R \equiv \lambda/\delta\lambda$). The Space Telescope Imaging Spectrograph (STIS; Kimble et al. 1998; Woodgate et al. 1998) spectra were obtained through the Mikulski Archive for Space Telescopes (MAST) and processed automatically by the CALSTIS pipeline. The High Accuracy Radial velocity Planet Searcher (HARPS; Mayor et al. 2003) spectra and Ultraviolet Visual Echelle Spectrograph (UVES; Dekker et al. 2000) spectra were obtained through the European Southern Observatory Science Archive Facility. The High Resolution Echelle Spectrometer (HIRES; Vogt et al. 1994) spectra were obtained through the Keck Observatory Archives. The Magellan Inamori Kyocera Echelle (MIKE; Bernstein et al. 2003) spectra and Robert G. Tull Coudé (Tull et al. 1995) spectra have been collected over the years by us. We use the Image Reduction and Analysis Facility (IRAF; Tody 1993) software to shift to rest velocity, co-add, and continuum normalize the spectra.

Figure 1 illustrates a region around the Al II line in the STIS spectra of all 11 stars in our sample. Typical signal-to-noise (S/N) ratios near the Al II line range from 40 to 70 pix^{-1} , except for the spectra of HD 108317 and HD 128279, where $S/N \approx 160 \text{ pix}^{-1}$. Figure 1 illustrates that this line remains largely free of blends, even in the coolest and most metal-rich stars in the sample. The Al II line with the lowest detection significance, 3.5σ ,

Table 2. Atomic Data for Lines Used in This Study

Species	λ (Å)	E.P. (eV)	$\log(gf)^a$	Grade ^b	HFS ^a
Al I	2118.332	0.00	-1.56	C	...
Al I	2129.678	0.00	-1.38	C	...
Al I	2199.180	0.00	-2.60	C	VALD
Al I	2204.660 ^c	0.00	-0.90	C+	...
Al I	2263.738	0.01	-1.94	C	VALD
Al I	2269.220	0.01	-1.41	C+	...
Al I	2372.070	0.00	-2.01	C	VALD
Al I	2373.122	0.01	-0.34	B	VALD
Al I	2567.982	0.00	-1.12	B	VALD
Al I	3944.006	0.00	-0.64	B+	VALD
Al I	3961.519	0.01	-0.33	B+	VALD
Al I	6696.019	3.14	-1.57	C+	VALD
Al I	6698.670	3.14	-1.87	C+	VALD
Al I	7835.309	4.02	-0.69	B	...
Al I	7836.134 ^d	4.02	-0.53	B+	...
Al II	2669.155	0.00	-4.98	A+	This study

^aSee text for references.

^b $\log(gf)$ grade assigned in the NIST ASD (A+ = 2%, A = 3%, B+ = 7%, B = 10%, C+ = 18%, C = 25%).

^cLine blends together with the weaker Al I line at 2204.619 Å, with E.P. = 0.01 eV, $\log(gf) = -2.29$, grade “C,” and HFS from VALD.

^dLine blends together with the weaker Al I line at 7836.134 Å, with E.P. = 4.02 eV, $\log(gf) = -1.83$, and grade “C+.”

is found in BD +03°740. All other detections are 8σ significance or greater.

S/N ratios around Al I lines are $\gtrsim 30 \text{ pix}^{-1}$ at 2200 Å and increase to longer wavelengths. More extensive lists of S/N ratios at a variety of UV and optical wavelengths for these spectra can be found in Table 1 of [Roederer](#)

(2012), Table 2 of [Roederer et al. \(2012\)](#), Section 2 of [Roederer et al. \(2014b\)](#), Table 1 of [Roederer et al. \(2018b\)](#), and Section 3 of [Peterson et al. \(2020\)](#).

Table 3. Log of Observations

Star	Instrument	Program ID	MAST Datasets	PI	λ (Å)	R
BD +03°740	STIS	GO-14232	OCTS01010-2030	Roederer	2278–3068	30,000
	MIKE	<i>a</i>	...	Roederer	3340–9410	42,000
BD +44°493	STIS	GO-12554	OBQ603010-4040	Beers	2278–3073	30,000
	Tull	<i>b</i>	...	Roederer	3636–8000	33,000
HD 19445	STIS	GO-7402	O56D01010-3010	Peterson	2313–3067	30,000
	UVES	66.D-0636(A)	...	Piotto	3760–4980	41,000
	UVES	68.D-0094(A)	...	Primas	5841–6810	51,000
HD 84937	STIS	GO-14161	OCTKA0010-D01030	Peterson	1879–3143	114,000
	UVES	073.D-0024(A)	...	Akerman	3757–4980	54,000
	UVES	266.D-5655(A)	...	<i>c</i>	5836–6809	74,000
HD 94028	STIS	GO-8179	O5CN01010-3040	Duncan	1879–2148	114,000
	STIS	GO-14161	OCTKB0010-6030	Peterson	2128–3143	114,000
	Tull	<i>b</i>	...	Roederer	3647–8000	33,000
HD 108317	STIS	GO-12268	OBJQ01010-3050	Roederer	2280–3115	30,000
	STIS	GO-12976	OBXV01010-4030	Roederer	1610–2365	30,000
	MIKE	<i>b</i>	...	Thompson	3340–8000	41,000
HD 128279	STIS	GO-12268	OBJQ04010-6050	Roederer	2280–3115	30,000
	STIS	GO-12976	OBXV05010-7050	Roederer	1610–2365	30,000
	MIKE	<i>b</i>	...	Thompson	3340–8000	41,000
HD 140283	STIS	GO-7348	O55Z01010-2070	Edvardsson	1932–2212	114,000
	STIS	GO-9455	O6LM71010-40	Peterson	2390–3140	51,000
	HARPS	080.D-0347(A)	...	Heiter	3784–6917	115,000
HD 175305	STIS	GO-8342	O5F609010 ^d	Cowan	2277–3119	30,000
	Tull	<i>b</i>	...	Roederer	3679–8000	33,000
HD 196944	STIS	GO-12554	OBQ601010-30	Beers	2278–3073	30,000
	STIS	GO-14765	OD5A01010-14010	Roederer	2029–2303	114,000
	MIKE	<i>b</i>	...	Roederer	3350–9150	41,000
HD 222925	STIS	GO-15657	ODX901010-60030	Roederer	1936–3145	114,000
	MIKE	<i>e</i>	...	Roederer	3330–9410	66,000

Table 3 *continued*

Table 3 (continued)

Star	Instrument	Program ID	MAST Datasets	PI	λ (Å)	R
------	------------	------------	---------------	----	---------------	-----

^aPreviously unpublished spectrum collected 2019 October 24

^bSee Roederer et al. (2014a)

^cUVES Paranal Observatory Project (Bagnulo et al. 2003)

^dVia StarCat (Ayres 2010)

^eSee Roederer et al. (2018a)

4. ANALYSIS

4.1. Model Atmospheres

We adopt the model parameters (effective temperature, T_{eff} ; log of the surface gravity, $\log g$; microturbulent velocity parameter, v_t ; and model metallicity, $[M/H]$) derived previously for these stars. We interpolate model atmospheres from the 1D, α -enhanced ATLAS9 grid of models (Castelli & Kurucz 2004). These values are listed in Table 4.

4.2. Fe Abundances

We derive abundances using a recent version of the MOOG line analysis software (Snedden 1973, 2017 version). MOOG assumes that LTE holds in the line-forming layers of the atmosphere. This version of MOOG accounts for Rayleigh scattering, which affects the continuous opacity at shorter wavelengths, as isotropic, coherent scattering (Sobeck et al. 2011).

We derive Fe abundances using Fe II lines, which are less susceptible than Fe I lines to departures from LTE. We update previously-derived abundances to the Fe II $\log(gf)$ scale established by Den Hartog et al. (2019). If an Fe II line is not present in the Den Hartog et al. list, we adopt the $\log(gf)$ value from Meléndez & Barbuy (2009), if available, otherwise we default to the recommended NIST value. We discard any Fe II lines in the “Balmer Dip” region ($\approx 3100\text{--}3700$ Å), where multiple 1D LTE line analysis codes yield abundances that are systematically different from those derived using lines at shorter and longer wavelengths (Roederer et al. 2018b). Our updated $[\text{Fe}/\text{H}]$ ratios are listed in Table 4. The mean changes are $\leq +0.05$ dex for all stars except HD 94028, for which the change is $+0.09$ dex. These small changes would have had a negligible impact on the model atmospheres derived previously. Nearly all previous studies derived $\log g$, the one parameter potentially most sensitive to Fe II lines, using distances from parallax measurements rather than Fe ionization balance. The two stars whose $\log g$ values were derived using the Fe ionization balance method, BD +44°493 and HD 196944, are unaffected because their updated Fe abundances changed by ≤ 0.01 dex.

4.3. Al Abundances

We derive Al abundances by matching synthetic spectra to the observed spectra. We generate line lists for synthesis with our own version of the ‘linemake’ software¹, which includes updates relevant to the UV spectral range. Figure 2 illustrates these fits to the Al II line. This line remains on the linear part of the curve-of-growth in most stars in our sample. We also derive Al abundances from Al I lines. Not all Al I lines are detectable or useful as abundance indicators in each star. The lines from the ground level, while nearly always present in these spectra, are frequently saturated or blended with other species. The Al I line at 3944 Å, for example, is frequently blended with CH lines (Arpigny & Magain 1983), and it is useful as an abundance indicator only in a few warm, metal-poor stars without enhanced carbon. The high-excitation lines are only detectable in the most metal-rich stars in our sample. Table 5 lists the abundance derived from each line.

Following Roederer et al. (2018a), we compute 1σ abundance uncertainties as follows. We draw 250 resamples of the stellar parameters (with assumed uncertainties of 100 K in T_{eff} , 0.2 dex in $\log g$, 0.2 km s⁻¹ in v_t , and 0.2 dex in $[M/H]$), $\log(gf)$ values (with uncertainties quoted in the original source references or NIST ASD), and equivalent widths approximated from the abundance derived via synthesis using a reverse curve-of-growth method (with assumed 5%, or minimum 2 mÅ, uncertainties). We recompute the $\log \varepsilon$ Al and Fe abundances and the $[\text{Al}/\text{Fe}]$ ratio for each resample. Each distribution is roughly symmetric, and we adopt the 16th and 84th percentiles as the 1σ uncertainty on each quantity.

5. RESULTS

Table 6 lists the weighted mean $\log \varepsilon(\text{Al})$ abundances and $[\text{Al}/\text{Fe}]$ ratios, based on Al II and Fe II lines. For these 11 stars spanning $-3.9 < [\text{Fe}/\text{H}] < -1.3$, the weighted mean $[\text{Al}/\text{Fe}]$ is -0.06 ± 0.04 ($\sigma = 0.22$). If two well-known carbon-enhanced stars (BD +44°493 and HD 196944; see, e.g., Ito et al. 2013 and Placco et al. 2015) are excluded, the weighted mean $[\text{Al}/\text{Fe}]$ ra-

¹ <https://github.com/vmplacco/linemake>

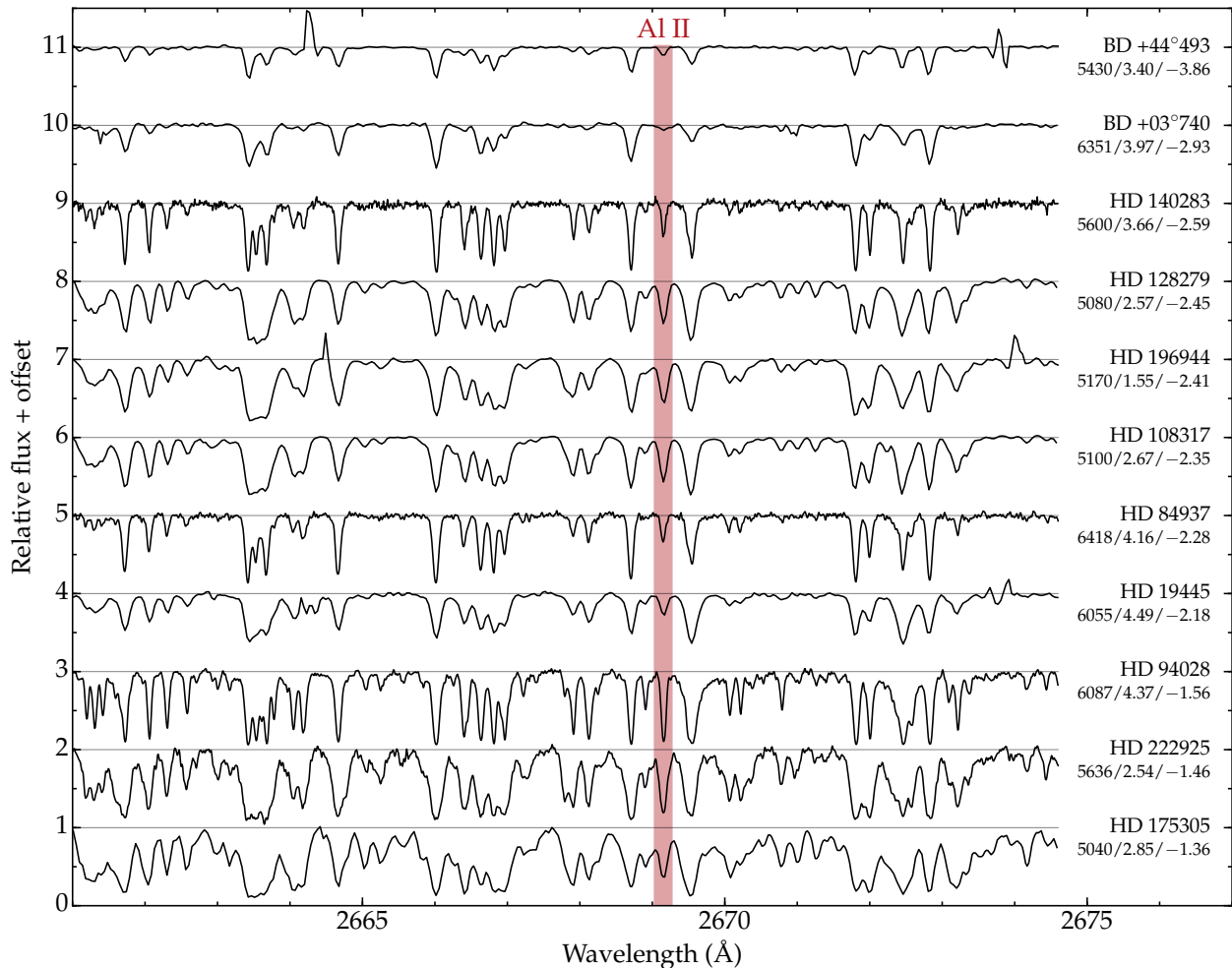


Figure 1. Sections of the STIS spectra. The Al II line at 2669.155 Å is marked by the shaded box. Thin gray lines mark the approximate continuum in each star. The spectra have been shifted vertically for display purposes, and they are ordered by increasing $[\text{Fe}/\text{H}]$ from top to bottom. The star names and $T_{\text{eff}}/\log g/[\text{Fe}/\text{H}]$ values (in units of K, $\log \text{cm s}^{-2}$, and dex) are listed.

to spanning $-3.0 < [\text{Fe}/\text{H}] < -1.3$ is -0.10 ± 0.04 ($\sigma = 0.18$).

5.1. Comparison of Al Abundances from Different Lines

Figure 3 illustrates the relative Al abundances derived from different lines. The Al I resonance lines yield consistent abundances in each star. The high-excitation Al I lines and the Al II line also yield consistent abundances in each star. These lines yield different abundances, however, in the sense that the abundances derived from Al I resonance lines are lower than those derived from high-excitation Al I lines and the Al II line.

Figure 4 illustrates these differences, defined as the $[\text{Al}/\text{H}]$ ratio derived from the Al II line minus the $[\text{Al}/\text{H}]$ ratio derived from the Al I resonance lines, as a function of T_{eff} , $\log g$, and $[\text{Fe}/\text{H}]$. The differences range from $\approx +0.4$ to $+0.9$ dex. The minimal differences between the coolest and warmest stars in our sample recalls ear-

lier results by Ryan et al. (1996), Norris et al. (2001), and Andrievsky et al. (2008), where the $[\text{Al}/\text{Fe}]$ trends exhibited similar behavior in both dwarfs and giants.

5.2. Comparison of LTE Al Abundances with Previous Studies

Our stellar sample overlaps with two modern NLTE Al abundance studies. We compare their LTE abundances, derived from the Al I resonance lines, to ours, as a consistency check of our results. We also compare our LTE Al abundance with that derived previously for the most metal-poor star in our sample.

There are two stars in common between our study and Zhao et al. (2016), HD 84937 and HD 94028. Our LTE $[\text{Al}/\text{H}]$ ratios differ from theirs by $+0.04$ and $+0.21$ dex, respectively. We have no lines in common with Zhao et al. If we rederive Al abundances from the UV Al I resonance lines using the Zhao et al. model atmosphere parameters, our $[\text{Al}/\text{H}]$ ratios agree to within 0.02 dex

Table 4. Model Atmosphere Parameters

Star	T_{eff} (K)	$\log g$ [cgs]	v_t (km s $^{-1}$)	[M/H]	[Fe/H] ^a	References
BD +03°740	6351	3.97	1.70	-2.90	-2.93	Roederer et al. (2018b)
BD +44°493	5430	3.40	1.30	-3.80	-3.86	Ito et al. (2013); Placco et al. (2014)
HD 19445	6055	4.49	1.20	-2.20	-2.18	Roederer et al. (2018b)
HD 84937	6418	4.16	1.50	-2.25	-2.28	Roederer et al. (2018b)
HD 94028	6087	4.37	1.10	-1.60	-1.56	Roederer et al. (2018b)
HD 108317	5100	2.67	1.50	-2.37	-2.35	Roederer et al. (2012)
HD 128279	5080	2.57	1.60	-2.46	-2.45	Roederer et al. (2012)
HD 140283	5600	3.66	1.15	-2.62	-2.59	Roederer (2012)
HD 175305	5040	2.85	2.00	-1.48	-1.36	Cowan et al. (2005)
HD 196944	5170	1.60	1.55	-2.41	-2.41	Placco et al. (2015)
HD 222925	5636	2.54	2.20	-1.50	-1.46	Roederer et al. (2018a)

^a[Fe/H] derived from Fe II lines on the $\log(gf)$ scale described in the text.

and 0.10 dex. Both values are within the stated abundance uncertainties.

There are also two stars in common between our study and Nordlander & Lind (2017), HD 84937 and HD 140283. Our 1D LTE Al abundances derived from the resonance lines differ from theirs by +0.09 and -0.20 dex, respectively. Our model atmosphere parameters are very similar for HD 84937, and our Al abundances decrease by only -0.01 dex if we adopt their model atmosphere parameters. The resulting [Al/H] ratios differ by only +0.08 dex, which is within the stated uncertainties. For HD 140283, we adopt a model atmosphere with a cooler T_{eff} (5600 K) than Nordlander & Lind did (5777 K). The warmer value is supported by interferometric measurements of the radius by Karovicova et al. (2018, 2020), but we adopt the cooler value for consistency with our previous work. The [Al/H] abundance difference shrinks to only +0.04 dex if we instead adopt their model, and this difference is well within the uncertainties.

BD +44°493 is the most metal-poor star in our sample, and no NLTE Al abundances have been published for this star. Ito et al. (2009) derived an LTE abundance $\log \varepsilon(\text{Al}) = 2.06$ from the Al I line at 3961 Å, which is in excellent agreement with the LTE abundance we derive from this line, $\log \varepsilon(\text{Al}) = 2.05$. We confirm this abundance using two additional Al I lines in the UV.

In summary, our LTE Al abundances derived from Al I lines are in agreement with previous studies of the same stars.

6. DISCUSSION

6.1. A Test of NLTE Calculations

Many previous studies, including Baumüller & Gehren (1997), Andrievsky et al. (2008), Menzhevitski et al. (2012), Mashonkina et al. (2016), and Nordlander & Lind (2017), have discussed the impact of NLTE on neutral Al in metal-poor stars. NLTE photoionization from the ground level of neutral Al is responsible for the low LTE Al abundances derived from Al I resonance lines. The Al neutral atom high-excitation levels are more closely coupled to the ground level of the ion by resonant charge transfer reactions involving H^- , so lines from these levels are formed near LTE. There is some variation among NLTE calculations, even those that use identical atomic and collisional data (Belyaev 2013), concerning the magnitude of the corrections (see, e.g., discussion in Nordlander & Lind). In general, however, for metal-poor stars the NLTE abundance corrections to the resonance lines are positive and large, $\approx +0.3$ to $+0.8$ dex for $T_{\text{eff}} > 5000$ K and/or $\log g < 4.0$, depending on the exact combination of stellar parameters. The NLTE abundance corrections to the high-excitation lines are usually small, ≈ 0.1 dex or less. Figures 14 and 15 of Nordlander & Lind illustrate the NLTE corrections from that study and several others for comparison.

Previous studies (e.g., Mashonkina et al. 2016) have also shown that the ground state of Al^+ , which gives rise to the Al II line studied here, is formed in LTE. We conclude that the difference between the LTE Al abundance derived from the Al II line and the LTE Al abundance derived from the Al I resonance lines, shown in Figure 4, presents an independent estimate of the NLTE corrections. Our results therefore indicate that the NLTE calculations are approximately correct for the stellar parameter range reflected in our sample ($5000 < T_{\text{eff}} < 6500$ K; $1.5 < \log g < 4.5$; $-3.9 < [\text{Fe}/\text{H}] < -1.3$). For

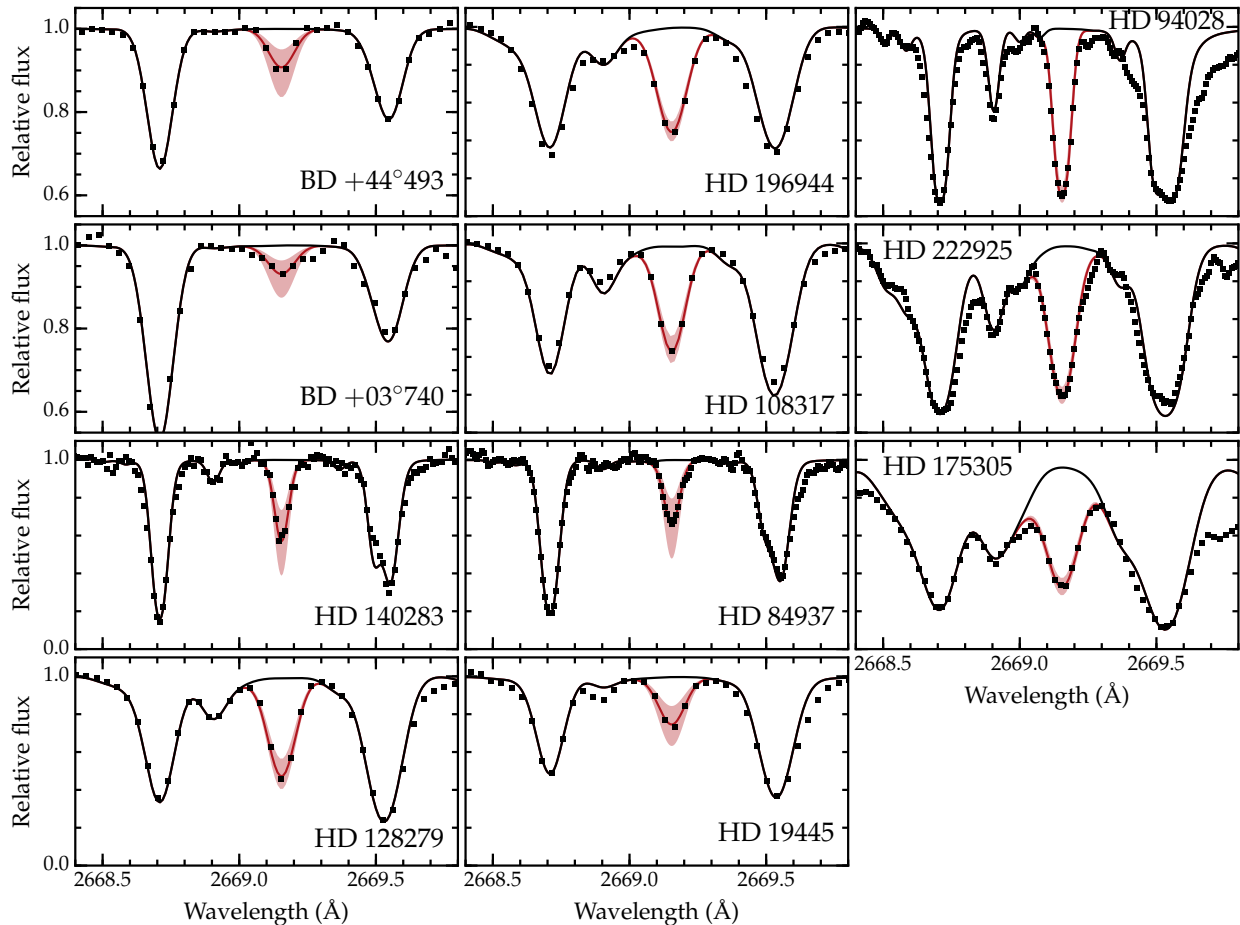


Figure 2. Comparison of synthetic and observed spectra around the Al II line. The filled dots mark the observed spectra. The red solid lines represent synthetic spectra with the best-fit Al abundance, and the pink bands represent changes in this abundance by factors of ± 2 (0.3 dex). The black lines represent synthetic spectra with no Al. The panels are ordered by increasing $[\text{Fe}/\text{H}]$.

example, Nordlander & Lind (2017) calculated NLTE corrections to the Al I line at 3961 Å of $\approx +0.5$ to $+0.8$ dex for metal-poor giants ($T_{\text{eff}} = 5250$ K; $-4.0 \leq [\text{Fe}/\text{H}] \leq -1.3$) or $\approx +0.4$ to $+0.6$ dex for metal-poor turnoff stars ($T_{\text{eff}} = 6250$ K; $-4.0 \leq [\text{Fe}/\text{H}] \leq -1.3$), which match our results. This agreement offers a gratifying confirmation of the NLTE predictions.

6.2. The $[\text{Al}/\text{Fe}]$ Ratio in Metal-Poor Stars

Figure 5 illustrates the $[\text{Al}/\text{Fe}]$ ratio as a function of $[\text{Fe}/\text{H}]$ for the 11 stars in our sample. NLTE $[\text{Al}/\text{Fe}]$ ratios derived from Al I lines (Andrievsky et al. 2008; Zhao et al. 2016; Nordlander & Lind 2017) are shown for comparison. Figure 5 demonstrates that our LTE $[\text{Al}/\text{Fe}]$ ratios, derived from Al II and Fe II lines, are in good agreement with the NLTE $[\text{Al}/\text{Fe}]$ ratios derived previously.

The $[\text{Al}/\text{Fe}]$ ratio is roughly constant and slightly subsolar across the metallicity range examined. This result is in reasonable agreement with predictions of

Galactic chemical evolution models. The best model of Kobayashi et al. (2020), for example, predicts only a modest rise in $[\text{Al}/\text{Fe}]$ from -0.3 to $+0.2$ from $[\text{Fe}/\text{H}] = -4$ to -1 , as shown in Figure 5.

The mild tension appears most pronounced at the lowest metallicities, where inhomogeneous chemical enrichment could be expected to bias the results in small samples. BD +44°493 is the most metal-poor star in our sample. It is a carbon-enhanced metal-poor star with no enhancement of neutron-capture elements (CEMP-no star; e.g., Ito et al. 2009; Placco et al. 2014). The $[\text{Al}/\text{Fe}]$ ratio we derive using the Al II line, $+0.33 \pm 0.13$, is higher by $+0.9$ dex than the $[\text{Al}/\text{Fe}]$ ratio derived previously by Ito et al., -0.57 ± 0.15 . We attribute this discrepancy to NLTE overionization of neutral Al. Enhanced $[\text{Al}/\text{Fe}]$ ratios are found in $\sim 50\%$ of CEMP-no stars, and frequently they are correlated with enhanced $[\text{Na}/\text{Fe}]$, $[\text{Mg}/\text{Fe}]$, and $[\text{Si}/\text{Fe}]$ ratios (e.g., Norris et al. 2013). Ito et al. (2013) find similar levels of enhancement, ranging from $+0.30$ to $+0.49$, among these three

Table 5. Abundances Derived from Individual Lines

Star	Al I	Al I	Al I	Al I	Al I	Al I	Al I	Al I	Al I	Al I	Al I	Al I	Al I	Al I	Al I	Al II
	2118	2129	2199	2204	2263	2269	2372	2373	2567	3944	3961	6696	6698	7835	7836	2669
	log ϵ abundance															
BD +03°740	2.90	3.02	3.00	2.73	3.52
BD +44°493	2.02	2.22	...	2.05	2.92
HD 19445	3.94	3.87	3.50	3.72	4.25
HD 84937	3.53	3.65	...	3.65	3.63	3.68	3.80	3.42	3.59	3.50	4.20
HD 94028	4.83	...	4.68	...	4.60	4.74	4.84	...	4.68	5.18
HD 108317	3.33	...	3.19	3.20	3.25	3.33	3.22	3.22	3.90
HD 128279	3.15	3.36	3.33	3.40	3.21	3.16	3.72
HD 140283	2.87	2.94	3.27	3.02	2.69	3.00	3.00	...	2.83	3.65
HD 175305	4.21	5.01	4.95	4.76
HD 196944	3.20	3.27	...	3.21	3.16	3.22	3.28	4.16
HD 222925	4.32	4.28	4.27	4.21	4.12	4.27	4.17	...	4.20	4.87	4.90	...	4.63	4.77
	Fitting uncertainty in log ϵ abundance															
BD +03°740	0.10	0.15	0.10	0.15	0.10
BD +44°493	0.10	0.10	...	0.10	0.05
HD 19445	0.15	0.15	0.15	0.15	0.05
HD 84937	0.10	0.10	...	0.10	0.15	0.10	0.15	0.15	0.10	0.05	0.05
HD 94028	0.20	...	0.15	...	0.10	0.15	0.10	...	0.15	0.20
HD 108317	0.15	...	0.25	0.15	0.15	0.20	0.15	0.15	0.15
HD 128279	0.25	0.15	0.15	0.20	0.15	0.15	0.15
HD 140283	0.10	0.10	0.20	0.10	0.25	0.10	0.10	...	0.10	0.05
HD 175305	0.15	0.25	0.15	0.20
HD 196944	0.10	0.10	...	0.10	0.05	0.10	0.15	0.15
HD 222925	0.15	0.15	0.15	0.10	0.10	0.10	0.15	...	0.15	0.20	0.20	...	0.20	0.10

ratios in BD +44°493. The super-solar [Al/Fe] ratio also improves the zero-metallicity supernova model fits to the abundance pattern in BD +44°493 (Tominaga et al. 2014; Roederer et al. 2016). The enhanced [Al/Fe] ratio in BD +44°493 may not be representative, however, of the [Al/Fe] ratio in extremely metal-poor stars without excesses of carbon and other light elements. New data based on the Al II line in such stars would be welcome.

7. SUMMARY

We present Al abundances using, for the first time, an Al II line, detected at 2669 Å in HST/STIS spectra of 11 metal-poor stars that span $5000 < T_{\text{eff}} < 6500$ K, $1.5 < \log g < 4.5$, and $-3.9 < [\text{Fe}/\text{H}] < -1.3$. This line is formed in LTE, and the Al abundances derived from this line, and Fe abundances derived from Fe II lines, yield [Al/Fe] ratios that are slightly sub-solar, -0.06 ± 0.04 ($\sigma = 0.22$). This value is in good agreement with previous studies that have made use of NLTE calculations

to derive Al abundances from Al I lines in optical and infrared spectra.

The detection of this line enables a new test of NLTE calculations of Al I resonance lines that are not formed in LTE. The differences between the Al abundance derived from this Al II line and the Al abundances derived from Al I resonance lines, $\approx +0.4$ to $+0.9$ dex, match the predicted NLTE corrections to LTE abundances derived from the Al I resonance lines. The agreement is highly encouraging. Whenever spectra covering the UV Al II line are unavailable—as is the case for the vast majority of stars at present—the NLTE corrections to LTE abundances should be considered reliable when applied on a line-by-line and star-by-star basis.

In future decades, the UV Al II line at 2669 Å will be an important abundance indicator of Al nucleosynthesis in the first generations of stars. It lies in a clean spectral window in metal-poor stars. It is detectable in stars with metallicity at least as low as $[\text{Fe}/\text{H}] \simeq -4$, and it should

Table 6. Mean Abundances

Star	Al I (resonance)		Al I (high exc.)		Al II		[Fe/H] ^a	[Al/Fe] ^b
	log ϵ	N	log ϵ	N	log ϵ	N		
BD +03° 740	2.93 ± 0.10	4	3.52 ± 0.17	1	-2.93 ± 0.08	+0.00 ± 0.17
BD +44° 493	2.09 ± 0.13	3	2.92 ± 0.22	1	-3.86 ± 0.16	+0.33 ± 0.13
HD 19445	3.74 ± 0.10	4	4.25 ± 0.10	1	-2.18 ± 0.07	-0.02 ± 0.08
HD 84937	3.56 ± 0.10	9	4.20 ± 0.10	1	-2.28 ± 0.10	+0.03 ± 0.11
HD 94028	4.72 ± 0.11	6	5.18 ± 0.20	1	-1.56 ± 0.09	+0.29 ± 0.20
HD 108317	3.25 ± 0.14	7	3.90 ± 0.15	1	-2.35 ± 0.12	-0.20 ± 0.15
HD 128279	3.26 ± 0.13	6	3.72 ± 0.15	1	-2.45 ± 0.10	-0.28 ± 0.15
HD 140283	2.94 ± 0.12	8	3.65 ± 0.11	1	-2.59 ± 0.08	-0.21 ± 0.09
HD 175305	4.21 ± 0.17	1	4.97 ± 0.17	2	4.76 ± 0.20	1	-1.36 ± 0.10	-0.33 ± 0.20
HD 196944	3.22 ± 0.16	6	4.16 ± 0.18	1	-2.41 ± 0.08	+0.12 ± 0.19
HD 222925	4.23 ± 0.11	8	4.79 ± 0.22	3	4.77 ± 0.13	1	-1.46 ± 0.11	-0.22 ± 0.13

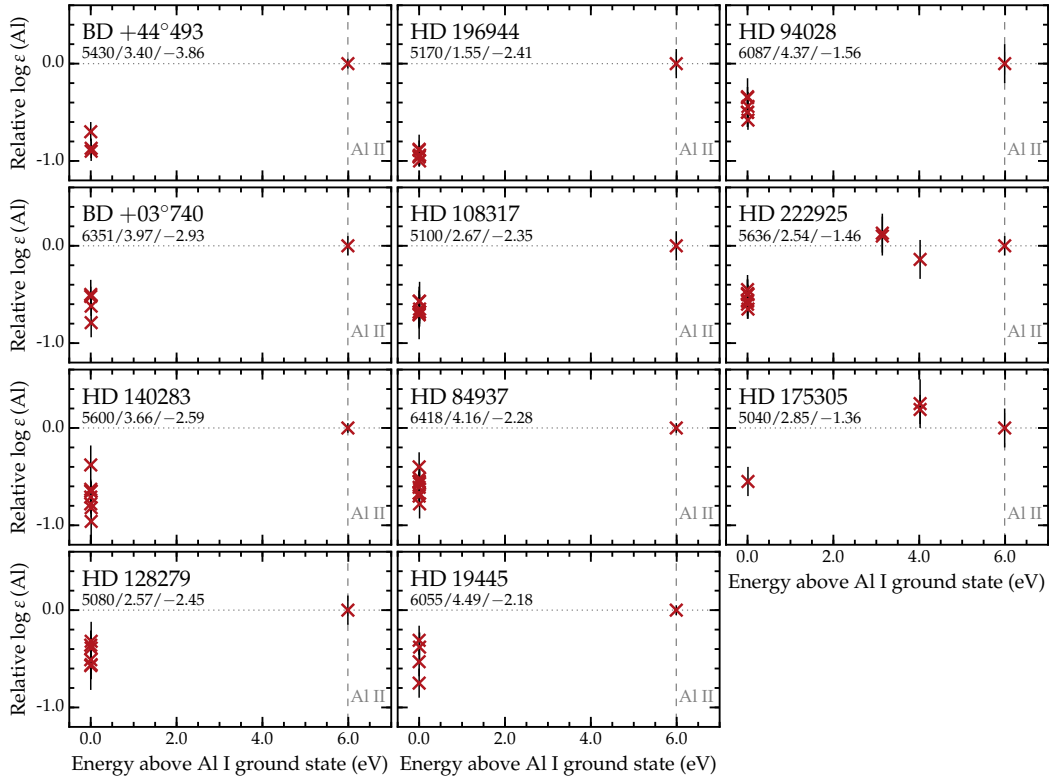
^aDerived from Fe II lines^bDerived from Al II and Fe II lines

Figure 3. Comparison of Al abundances derived from different lines. The crosses mark abundances derived from individual lines. Each set of abundances is scaled relative to the abundance derived from the Al II line at 2669 Å, whose value is indicated as a dotted line at zero. The first ionization potential of Al, 5.99 eV, is indicated by the vertical dashed line. The $T_{\text{eff}}/\log g$ /[Fe/H] values (in units of K, $\log \text{cm s}^{-2}$, and dex) are listed. The panels are ordered by increasing [Fe/H].

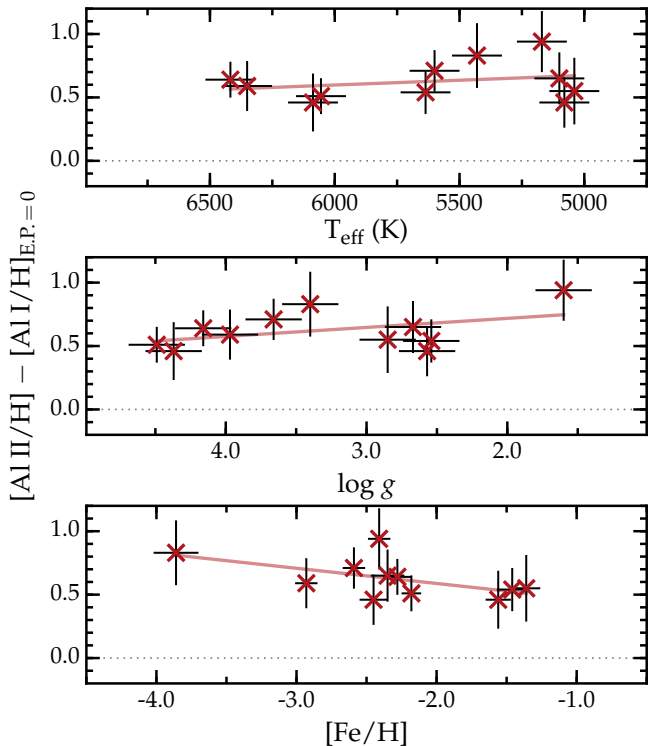


Figure 4. Comparison of Al abundance differences between those derived from the Al II line at 2669 Å and the Al I resonance lines. Linear fits are shown. The dotted line marks a difference of zero.

be detectable when $[Al/H] > -5$ in cool giants. UV observations at this wavelength are feasible with STIS and any of the future space missions with a high-resolution UV spectrograph that have been proposed to NASA, including the Habitable Exoplanet Observatory (HabEx; Gaudi et al. 2020), the Large UV/Optical/Infrared Surveyor (LUVOIR; The LUVOIR Team 2019), and the Cosmic Evolution Through UV Surveys mission (CE-TUS; Heap et al. 2019).

ACKNOWLEDGMENTS

We thank Chiaki Kobayashi for sharing her chemical evolution model predictions, Shimon Kolkowitz for helpful discussions, Ian Thompson for taking two of the MIKE spectra, and the referee for a thoughtful

report. I.U.R. and J.E.L. acknowledge support provided by NASA through grants GO-14765 and GO-15657 from STScI, which is operated by the AURA under NASA contract NAS5-26555. I.U.R. also acknowledges financial support from grant PHY 14-30152 (Physics Frontier Center/JINA-CEE) and grant AST-1815403 awarded by the U.S. National Science Foundation (NSF). This research has made use of NASA’s

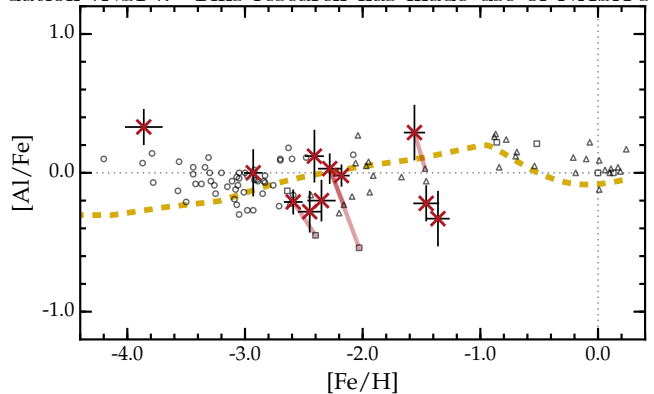


Figure 5. The $[Al/Fe]$ ratio as a function of $[Fe/H]$ for the stars in our sample and several previous studies. The large red crosses mark our abundances, derived from Al II and Fe II lines. The 1D NLTE results from previous studies are indicated by small gray circles (Andrievsky et al. 2008), small gray triangles (Zhao et al. 2016), and small gray squares (Nordlander & Lind 2017). The pink lines connect stars in common between our sample and previous work. The dashed yellow line marks the Galactic chemical evolution model presented by Kobayashi et al. (2020). The dotted lines mark the solar ratios.

Astrophysics Data System Bibliographic Services; the arXiv pre-print server operated by Cornell University; the SIMBAD and VizieR databases hosted by the Strasbourg Astronomical Data Center; the ASD hosted by NIST; the VALD, operated at Uppsala University, the Institute of Astronomy RAS in Moscow, and the University of Vienna; the MAST at STScI; and the IRAF software package.

Facility: ESO:3.6 m (HARPS), HST (STIS), Keck (HIRES), Magellan (MIKE), McDonald:Smith (Tull Coudé), VLT (UVES)

Software: IRAF (Tody 1993), matplotlib (Hunter 2007), MOOG (Snedden 1973), numpy (van der Walt et al. 2011), R (R Core Team 2013), scipy (Jones et al. 2001)

REFERENCES

- Andrievsky, S. M., Spite, M., Korotin, S. A., et al. 2008, A&A, 481, 481
- Arpigny, C., & Magain, P. 1983, A&A, 127, L7
- Asplund, M., Grevesse, N., Sauval, A. J., & Scott, P. 2009, ARA&A, 47, 481
- Arnett, W. D., & Thielemann, F. K. 1985, ApJ, 295, 589

- Ayres, T. R. 2010, *ApJS*, 187, 149
- Bagnulo, S., Jehin, E., Ledoux, C., et al. 2003, *The Messenger*, 114, 10
- Barklem, P. S., Piskunov, N., & O'Mara, B. J. 2000, *A&AS*, 142, 467
- Baumüller, D., & Gehren, T. 1997, *A&A*, 325, 1088
- Belfrage, C., Hörbäck, S., Levinson, C., et al. 1984, *Zeitschrift für Physik A Hadrons and Nuclei*, 316, 15
- Belyaev, A. K. 2013, *A&A*, 560, A60
- Bernstein, R., Shtetman, S. A., Gunnels, S. M., Mochnacki, S., & Athey, A. E. 2003, in *Proc. SPIE*, Vol. 4841, *Instrument Design and Performance for Optical/Infrared Ground-based Telescopes*, ed. M. Iye & A. F. M. Moorwood, 1694–1704
- Biemont, E., & Brault, J. W. 1987, *Physica Scripta*, 35, 286
- Brown, J. M., & Evenson, K. M. 1999, *Phys. Rev. A*, 60, 956
- Castelli, F., & Kurucz, R. L. 2004, *ArXiv e-prints*.
<https://arxiv.org/abs/astro-ph/0405087>
- Chang, E. S. 1990, *Journal of Physical and Chemical Reference Data*, 19, 119
- Chen, Y. Q., Nissen, P. E., Zhao, G., Zhang, H. W., & Benoni, T. 2000, *A&AS*, 141, 491
- Condon, E. U., & Shortley, G. H. 1935, *The Theory of Atomic Spectra* (Cambridge University Press, Cambridge)
- Cowan, J. J., Sneden, C., Roederer, I. U., et al. 2020, *ApJ*, 890, 119
- Cowan, J. J., Sneden, C., Beers, T. C., et al. 2005, *ApJ*, 627, 238
- Davidson, M. D., Volten, H., & Doenszelmann, A. 1990, *A&A*, 238, 452
- Dekker, H., D'Odorico, S., Kaufer, A., Delabre, B., & Kotzlowski, H. 2000, in *Proc. SPIE*, Vol. 4008, *Optical and IR Telescope Instrumentation and Detectors*, ed. M. Iye & A. F. Moorwood, 534–545
- Den Hartog, E. A., Lawler, J. E., Sneden, C., Cowan, J. J., & Brukhovetsky, A. 2019, *ApJS*, 243, 33
- Den Hartog, E. A., Lawler, J. E., Sneden, C., et al. 2021, *ApJ*, submitted
- Falkenberg, B., & Zimmermann, P. 1979, *Z. Naturforsch. A*, 34, 1249
- Francois, P. 1986, *A&A*, 160, 264
- Gaudi, B. S., Seager, S., Mennesson, B., et al. 2020, *arXiv e-prints*, arXiv:2001.06683.
<https://arxiv.org/abs/2001.06683>
- Gehren, T., Liang, Y. C., Shi, J. R., Zhang, H. W., & Zhao, G. 2004, *A&A*, 413, 1045
- Gratton, R. G., & Sneden, C. 1988, *A&A*, 204, 193
- Hannaford, P. 1999, *Microchemical Journal*, 63, 43
- Heap, S., Arenberg, J., Hull, T., Kendrick, S., & Woodruff, R. 2019, *arXiv e-prints*, arXiv:1909.10437.
<https://arxiv.org/abs/1909.10437>
- Hunter, J. D. 2007, *Computing in Science and Engineering*, 9, 90
- Itano, W. M., Bergquist, J. C., Bruschi, A., et al. 2007, in *Society of Photo-Optical Instrumentation Engineers (SPIE) Conference Series*, Vol. 6673, *Time and Frequency Metrology*, ed. R. J. Jones, 667303
- Ito, H., Aoki, W., Beers, T. C., et al. 2013, *ApJ*, 773, 33
- Ito, H., Aoki, W., Honda, S., & Beers, T. C. 2009, *ApJL*, 698, L37
- Jones, E., Oliphant, T., Peterson, P., & et al. 2001, *SciPy: Open source scientific tools for Python*, online.
<http://www.scipy.org/>
- Jönsson, G., Kröll, S., Lundberg, H., & Svanberg, S. 1984, *Zeitschrift für Physik A Hadrons and Nuclei*, 316, 259
- Karovicova, I., White, T. R., Nordlander, T., et al. 2020, *A&A*, 640, A25
- . 2018, *MNRAS*, 475, L81
- Kimble, R. A., Woodgate, B. E., Bowers, C. W., et al. 1998, *ApJL*, 492, L83
- Kobayashi, C., Karakas, A. I., & Lugaro, M. 2020, *ApJ*, 900, 179
- Kobayashi, C., Umeda, H., Nomoto, K., Tominaga, N., & Ohkubo, T. 2006, *ApJ*, 653, 1145
- Kramida, A., Ralchenko, Y., Reader, J., & NIST ASD Team. 2020, *NIST Atomic Spectra Database (ver. 5.8)*, [Online]. Available: <https://physics.nist.gov/asd>, National Institute of Standards and Technology, Gaithersburg, MD.
- Magain, P. 1987, *A&A*, 179, 176
- Mashonkina, L. I., Belyaev, A. K., & Shi, J. R. 2016, *Astronomy Letters*, 42, 366
- Mayor, M., Pepe, F., Queloz, D., et al. 2003, *The Messenger*, 114, 20
- McWilliam, A., Preston, G. W., Sneden, C., & Searle, L. 1995, *AJ*, 109, 2757
- Meléndez, J., & Barbuy, B. 2009, *A&A*, 497, 611
- Mendoza, C., Eissner, W., LeDourneuf, M., & Zeippen, C. J. 1995, *Journal of Physics B Atomic Molecular Physics*, 28, 3485
- Menzhevitski, V. S., Shimansky, V. V., & Shimanskaya, N. N. 2012, *Astrophysical Bulletin*, 67, 294
- Nordlander, T., & Lind, K. 2017, *A&A*, 607, A75
- Norris, J. E., Ryan, S. G., & Beers, T. C. 2001, *ApJ*, 561, 1034
- Norris, J. E., Yong, D., Bessell, M. S., et al. 2013, *ApJ*, 762, 28

- Pakhomov, Y. V., Ryabchikova, T. A., & Piskunov, N. E. 2019, *Astronomy Reports*, 63, 1010
- Peck, E. R., & Reeder, K. 1972, *Journal of the Optical Society of America (1917-1983)*, 62, 958
- Peterson, R. 1978, *ApJ*, 222, 595
- Peterson, R. C., Barbuy, B., & Spite, M. 2020, *A&A*, 638, A64
- Piskunov, N. E., Kupka, F., Ryabchikova, T. A., Weiss, W. W., & Jeffery, C. S. 1995, *A&AS*, 112, 525
- Placco, V. M., Beers, T. C., Roederer, I. U., et al. 2014, *ApJ*, 790, 34
- Placco, V. M., Beers, T. C., Ivans, I. I., et al. 2015, *ApJ*, 812, 109
- R Core Team. 2013, *R: A Language and Environment for Statistical Computing*, R Foundation for Statistical Computing, Vienna, Austria.
<http://www.R-project.org/>
- Roederer, I. U. 2012, *ApJ*, 756, 36
- Roederer, I. U., & Barklem, P. S. 2018, *ApJ*, 857, 2
- Roederer, I. U., & Lawler, J. E. 2012, *ApJ*, 750, 76
- Roederer, I. U., Placco, V. M., & Beers, T. C. 2016, *ApJL*, 824, L19
- Roederer, I. U., Preston, G. W., Thompson, I. B., et al. 2014a, *AJ*, 147, 136
- Roederer, I. U., Sakari, C. M., Placco, V. M., et al. 2018a, *ApJ*, 865, 129
- Roederer, I. U., Sneden, C., Lawler, J. E., et al. 2018b, *ApJ*, 860, 125
- Roederer, I. U., Lawler, J. E., Sobeck, J. S., et al. 2012, *ApJS*, 203, 27
- Roederer, I. U., Schatz, H., Lawler, J. E., et al. 2014b, *ApJ*, 791, 32
- Roederer, I. U., Lawler, J. E., Holmbeck, E. M., et al. 2020, *ApJL*, 902, L24
- Romano, D., Karakas, A. I., Tosi, M., & Matteucci, F. 2010, *A&A*, 522, A32
- Ryan, S. G., Norris, J. E., & Beers, T. C. 1996, *ApJ*, 471, 254
- Sneden, C., Cowan, J. J., Kobayashi, C., et al. 2016, *ApJ*, 817, 53
- Sneden, C. A. 1973, PhD thesis, The University of Texas at Austin.
- Sobeck, J. S., Kraft, R. P., Sneden, C., et al. 2011, *AJ*, 141, 175
- Spite, M., Peterson, R. C., Gallagher, A. J., Barbuy, B., & Spite, F. 2017, *A&A*, 600, A26
- Stück, H. L., & Zimmermann, P. 1970, *Zeitschrift für Physik*, 239, 345
- The LUVOIR Team. 2019, arXiv e-prints, arXiv:1912.06219. <https://arxiv.org/abs/1912.06219>
- Thielemann, F. K., & Arnett, W. D. 1985, *ApJ*, 295, 604
- Timmes, F. X., Woosley, S. E., & Weaver, T. A. 1995, *ApJS*, 98, 617
- Tody, D. 1993, in *Astronomical Society of the Pacific Conference Series*, Vol. 52, *Astronomical Data Analysis Software and Systems II*, ed. R. J. Hanisch, R. J. V. Brissenden, & J. Barnes, 173
- Tominaga, N., Iwamoto, N., & Nomoto, K. 2014, *ApJ*, 785, 98
- Träbert, E., Wolf, A., Linkemann, J., & Tordoir, X. 1999, *Journal of Physics B Atomic Molecular Physics*, 32, 537
- Tull, R. G., MacQueen, P. J., Sneden, C., & Lambert, D. L. 1995, *PASP*, 107, 251
- Unsöld, A. 1955, *Physik der Sternatmosphären*, MIT besonderer Berücksichtigung der Sonne. (Berlin, Springer)
- van der Walt, S., Colbert, S. C., & Varoquaux, G. 2011, *Computing in Science Engineering*, 13, 22
- Vogt, S. S., Allen, S. L., Bigelow, B. C., et al. 1994, in *Proc. SPIE*, Vol. 2198, *Instrumentation in Astronomy VIII*, ed. D. L. Crawford & E. R. Craine, 362
- Woodgate, B. E., Kimble, R. A., Bowers, C. W., et al. 1998, *PASP*, 110, 1183
- Woosley, S. E., & Weaver, T. A. 1995, *ApJS*, 101, 181
- Zhan-Kui, J., Lundberg, H., & Svanberg, S. 1982, *Physics Letters A*, 92, 27
- Zhang, T., Xie, L., Li, J., & Lu, Z. 2017, *PhRvA*, 96, 012514
- Zhao, G., Mashonkina, L., Yan, H. L., et al. 2016, *ApJ*, 833, 225